One-Pot Synthesis of Intermetallic Electrocatalysts in Ordered, Large-Pore Mesoporous Carbon/Silica toward Formic Acid Oxidation

Jongmin Shim,[†] Jaehyuk Lee,[†] Youngjin Ye,[†] Jongkook Hwang,[†] Soo-Kil Kim,[‡] Tae-Hoon Lim,[§] Ulrich Wiesner,[⊥] and Jinwoo Lee[†,*]

[†]Department of Chemical Engineering, Pohang University of Science and Technology (POSTECH), 77 Cheongam-ro, Nam-gu, Pohang 790-784, Korea, [‡]School of Integrative Engineering, Chung-Ang University, 84 Heukseok-ro, Dongjak-gu, Seoul 156-756, Korea, [§]Center for Fuel Cell Research, Korea Institute of Science and Technology, 5 Wolsong-gil, Sungbuk-gu, Seoul 136-791, South Korea, and [⊥]Department of Materials Science and Engineering, Cornell University, Ithaca, New York 14853, United States

ABSTRACT

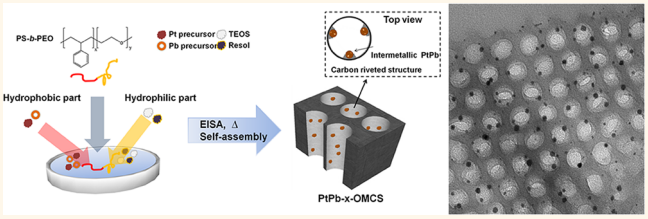

This study describes the one-pot synthesis and single-cell characterization of ordered, large-pore (>30 nm) mesoporous carbon/silica (OMCS) composites with well-dispersed intermetallic PtPb nanoparticles on pore wall surfaces as anode catalysts for direct formic acid fuel cells (DFAFCs). Lab-synthesized amphiphilic diblock copolymers coassemble hydrophobic metal precursors as well as hydrophilic carbon and silica precursors. The final materials have a two-dimensional hexagonal-type structure. Uniform and large pores, in which intermetallic PtPb nanocrystals are significantly smaller than the pore size and highly dispersed, enable pore backfilling with ionomers and formation of the desired triple-phase boundary in single cells. The materials show more than 10 times higher mass activity and significantly lower onset potential for formic acid oxidation as compared with commercial Pt/C, as well as high stability due to better resistivity toward CO poisoning. In single cells, the maximum power density was higher than that of commercial Pt/C, and the stability highly improved, compared with commercial Pd/C. The results suggest that PtPb-based catalysts on large-pore OMCSs may be practically applied as real fuel cell catalysts for DFAFC.

KEYWORDS: block copolymer · self-assembly · mesoporous structure · intermetallic nanoparticles · formic acid fuel cell

The direct formic acid fuel cell (DFAFC) has received significant attention as a promising energy source for portable electronic devices.[1−3] The use of formic acid as a fuel offers many advantages, compared with methanol, such as higher power density due to the low oxidation potential, better oxidation kinetics, and a lower crossover rate due to repulsive interactions between the Nafion membrane and formate anions.[4] Although notable progress in DFAFC research has been achieved in recent years, several issues such as poor performance of catalysts, long-term durability problems, and the high cost of noble metals have precluded the practical application of the DFAFC.

Pd and Pt catalysts have mainly been used as the anode catalyst for formic acid oxidation fuel cells.[5−8] The Pd catalyst exhibits a high initial activity based on the direct dehydrogenation pathway, which counters the CO poisoning effect, but loses catalytic activity rapidly over time.[9−13] On the other hand, the Pt catalyst is severely poisoned by absorbed CO, which is formed as a reaction intermediate *via* the undesirable dehydration pathway.[2,14−17] In order to overcome the limitations associated with Pd and Pt catalysts, researchers have employed various strategies including surface modification with adatoms[1,3,18,19] and the development of disordered alloys.[20,21] Work by Abruna, DiSalvo, *et al.* showed that unsupported intermetallic PtPb and PtBi phases are promising electrocatalysts for formic acid oxidation[22] in terms of both onset potential of oxidation and current density. These catalysts showed a higher tolerance to CO poisoning compared with Pt, PtRu, and Pd due to the combination of the same local geometry of Pt atoms and a larger Pt−Pt distance than that of the Pt-based alloys.[22,23] However, the original PtPb and PtBi intermetallic nanoparticles from Abruna, DiSalvo, *et al.* had large sizes and were highly agglomerated. In contrast, supported and highly dispersed intermetallic

* Address correspondence to jinwoo03@postech.ac.kr.

Received for review April 17, 2012 and accepted July 16, 2012.

Published online July 16, 2012
10.1021/nn301692y

nanocrystals are required for practical applications of Pt-based intermetallic nanocrystals. Nazar *et al*. reported the nucleated-growth synthesis of small-pore (~3 nm) ordered mesoporous carbon (OMC)-supported bimetallic PtBi catalysts by backfilling metal precursors followed by reduction at 350 °C.[24] Although they successfully prepared size-controlled and highly dispersed PtBi nanoparticles supported on small-pore CMK-3 type OMCs with good mass activity for formic acid oxidation, the demonstrated synthetic process using the hard-template method is tedious and cumbersome, *e.g*., requiring sulfur preloading for high dispersion of the PtBi nanoparticles.[24] Furthermore, only half-cell electrochemical reactions rather than single-cell behavior were reported in their work. Most likely, the pores are too small (<4 nm) to allow formation of a ubiquitous triple-phase boundary (TPB) during the membrane-electrode-assembly (MEA) fabrication process in a real fuel cell system (a single cell). Even nanoparticles as small as 2−3 nm leave only 1−2 nm of space for Nafion diffusion in pores of CMK-3 supports, thus effectively blocking the ionomer.[25] For effective charge (*e.g*., charge transfer through ionomers) and mass transfer, support materials such as OMCs[26] should have an optimized pore size of over 10 nm with high available surface area and interconnected pore structures. In addition, for practical applications the support materials loaded with catalyst nanoparticles should be simply fabricated with a minimum number of synthesis steps.

For all the aforementioned reasons, it is highly desirable to synthesize Pt-based intermetallic nanocrystals on a mesoporous carbon-type support with highly ordered pores (>10 nm) using a facile, "one pot" method. Compared with the backfilling method employing OMCs as catalyst supports, which requires at least 2 weeks, one-pot methods shorten the synthetic process time (5−6 days) and eliminate multiple tedious fabrication steps in the synthesis of Pt-based nanoparticles such as impregnation of pores with sulfur, followed by metal salts and subsequent heat treatment (Figure S1 in the Supporting Information).[27,28] Furthermore, in an amphiphilic block-copolymer directed one-pot synthesis hydrophobic metal precursors can be loaded exclusively into the hydrophobic part of the block copolymers due to favorable hydrophobic−hydrophobic interactions.[29] This optimized metal precursor choice leads to selective and exclusive deposition of the resulting Pt-based metal nanoparticles on the surface of the pores rather than within the pore walls of the carbon-based support. Although Orilall *et al*. synthesized a large-pore mesoporous niobium oxide−carbon composite incorporating Pt-based nanoparticles by using block copolymer poly(isoprene-*b*-ethylene oxide) (PI-*b*-PEO) as the structure-directing agent,[28] according to their XRD results the resulting nanoparticles did not exhibit an intermetallic phase. Furthermore, an expensive Nb-based oxide would not be desirable as the support material in real-world applications. Finally, in their work the ordered mesostructure was destroyed when reducing Nb_2O_5 to NbO_2 to get sufficient electrical conductivity, which diminishes the desired benefits of the ordered structure. Neither in the work by Orilall *et al*. nor in the work by Nazar *et al*. were materials tested in single-cell configurations.

Herein, we report the one-pot synthesis and single-cell characterization of highly dispersed intermetallic PtPb nanocrystals in ordered large-pore (>30 nm) mesoporous carbon−silica composites (PtPb-OMCS) having a 2-D hexagonal type structure. Lab-synthesized poly(styrene-*b*-ethylene oxide) (PS-*b*-PEO) is used to simultaneously direct hydrophobic metal precursors, as well as hydrophilic carbon and silicate precursors. We chose ordered mesoporous carbon−silica (OMCS) composites rather than OMCs as support as it is known that coexisting silica species in the walls are important to improve thermal and mechanical stability of the framework.[30] Besides, it is reported that silicate species are stable under polymer-electrolyte-membrane fuel cell (PEMFC) operation conditions.[31,32] The activity and stability of the resulting PtPb ordered intermetallic nanocrystals in large-pore OMCSs are compared with commercial Pt/carbon and Pd/carbon and are found to be superior. Single-cell performance is analyzed in order to demonstrate that the current PtPb-OMCSs catalyst can be practically applied in real fuel cells owing to the interconnected pores of the large-pore OMCSs. For practical applications in such tests the catalyst should outperform conventional Pt/C and Pd/C as a single-cell catalyst. As far as we are aware, such synthesis of materials for high-performance DFAFC anode applications has not been reported to date.

RESULTS AND DISCUSSION

Structural Characterization. 2-D, hexagonal, highly ordered, large-pore mesoporous carbon−silica composites with intermetallic PtPb nanoparticles (PtPb-*x*-OMCS; *x* represents the weight percentage of intermetallic PtPb nanoparticles based on the final carbon/silica composite) were prepared in organic solvents by coassembly of amphiphilic copolymer (PS-*b*-PEO) acting as a structure-directing agent, resol[33] as a carbon precursor, and tetraethylorthosilicate (TEOS) as a silica precursor and with metal precursors through an evaporation-induced self-assembly (EISA)[34,35] process (Figure 1). Laboratory-synthesized PS-*b*-PEO was selected as a structure-directing agent and was prepared *via* atom transfer radical polymerization,[36] a polymerization technique that makes block copolymer synthesis accessible to the nonexperts. The hydrophilic resols and oligomer silicate species having a number of −OH groups can interact strongly with the PEO block

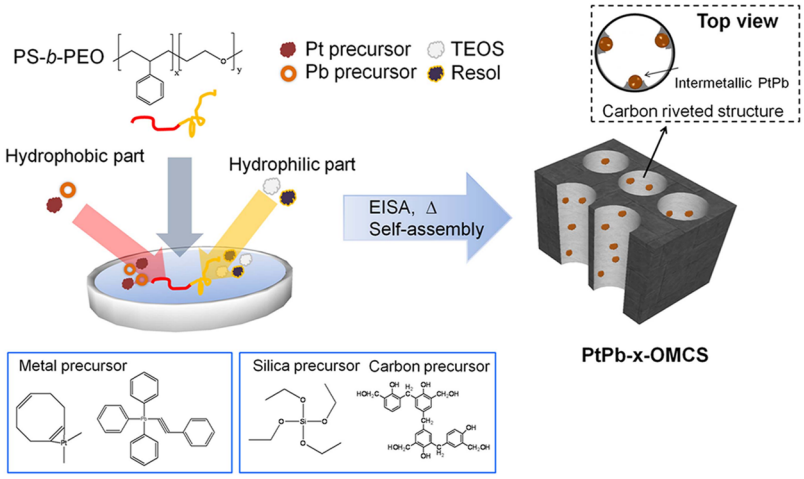

Figure 1. Schematic representation of the one-pot synthetic process for preparing intermetallic PtPb containing ordered large-pore mesoporous carbon−silica composites.

of the copolymer *via* hydrogen bonding, while the hydrophobic metal precursors selectively interact with the hydrophobic styrene segments. Precise control of the molar ratio of Pt and Pb precursors is crucial in the initial step of the experiment in order to produce the intermetallic PtPb phase by thermal reduction at 700 °C under a H_2/Ar atmosphere. During the EISA process at 50 °C, self-organization of the mixtures into ordered nanostructures close to equilibrium is induced by the block copolymers.[34] Following the thermal annealing process at 100 °C, the resol and silicates are polymerized, freezing the block copolymer mesostructure into the solid state.

The small-angle X-ray scattering (SAXS) patterns of the as-synthesized PtPb-*x*-OMCS (Figure 2a−c, black line) show several scattering peaks in a q range of 0.1−1.0. All of the as-synthesized PtPb-*x*-OMCS materials exhibit SAXS patterns with some combination of peak intensity ratios, q^m/q^*, of $1:3^{1/2}:4^{1/2}:9^{1/2}$, where q^* and q^m are the peak positions of the first and higher order maxima, respectively. Such a sequence is indicative of a well-ordered 2-D hexagonal mesostructure with long-range order. The corresponding $d_{spacing}$ values (d_{100}) of the first-order peaks (q^*) of the as-made PtPb-0-OMCS, PtPb-4.5-OMCS, and PtPb-9-OMCS samples are 35.2, 46.8, and 44.3 nm, respectively. The increase in the $d_{spacing}$ of PtPb-4.5-OMCS and PtPb-9-OMCS compared with PtPb-0-OMCS indicates that the hydrophobic metal precursors function not only as metal sources for PtPb intermetallic nanocrystals but also as pore expanders.[28,37] This expansion is beneficial for easy penetration of ionomers and facile formation of TPB with PtPb nanoparticles within the pores of the OMCS upon ionomer infiltration.

During heat treatment at 700 °C under mixed gas (4% H_2/Ar) atmosphere, the Pt and Pb precursors are thermally decomposed and converted into intermetallic PtPb, and the portion of the PS blocks that contains the sp^2-hybridized benzene ring is partially converted into rigid amorphous carbon, which lines the inner walls of the large-pore OMCS, and can prevent the size increase and agglomeration of nanoparticles.[38,39] Recently, carbon-riveted Pt nanoparticles were prepared on Vulcan XC-72 by coating standard Pt/Vulcan XC-72 with glucose to improve the stability of the Pt nanocatalyst.[40] In the synthetic system used in the present study, Pt and Pb precursors mixed with the polystyrene (PS) block of the block copolymer, which is converted to riveted carbon during the thermal decomposition, thus stabilizing the forming PtPb intermetallic nanocatalysts. Simultaneously, the PEO block mixed with the carbon and silica precursors is decomposed and consequently generates micropores in the resulting carbon−silica framework structure. Figure 3 shows Raman spectroscopy of three selected samples of OMC (without silica), PtPb-0-OMCS, and PtPb-4.5-OMCS. All of the Raman spectra display two broad peaks at around 1336 and 1600 cm^{-1}, corresponding to the D and G signals for carbons, respectively. The G-band is related to the stretching of sp^2-bonded carbon atoms in rings or chains. On the other hand, the D-band results from the breathing mode of sp^2-bonded carbon atoms in rings not chains.[41,42] This implies that self-assembled precursors (resol and part of PS) were successfully converted to conductive carbon materials. Although a lower temperature heat treatment is advantageous for the formation of small-sized Pb- or Pt-based nanoparticles,[43,44] powder XRD patterns of PtPb-OMCS heat-treated at 450 °C showed coexistence of Pt, Pb, and intermetallic PtPb phases (Figure S2 in the Supporting Information), indicating that heat treatment at 450 °C is insufficient for the full conversion of metal precursors into intermetallic PtPb nanoparticles. Therefore, we heat-treated our catalysts at 700 °C to obtain intermetallic PtPb nanoparticles. Furthermore, a higher temperature is required to obtain sufficient electrical conductivity of the carbon support (Figure S3 in the

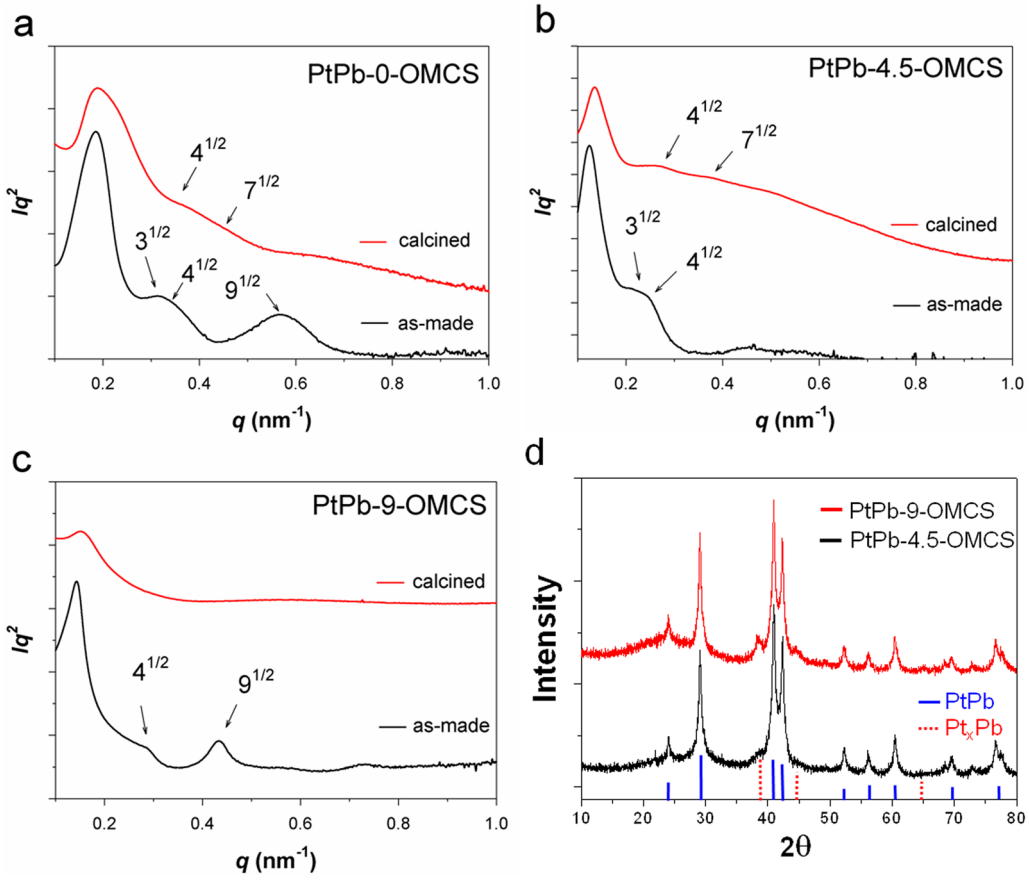

Figure 2. Characterization of materials by X-ray analysis. (a–c) SAXS patterns of ordered mesoporous carbon–silica composites as-made (black line) and calcined (red line): (a) PtPb-0-OMCS, (b) PtPb-4.5-OMCS, and (c) PtPb-9-OMCS. (d) Powder XRD patterns of calcined PtPb-4.5-OMCS (black line) and PtPb-9-OMCS (red line) overlaid with the reported peak positions and intensities of PtPb intermetallics (blue, solid line) and Pt_xPb (red, dotted line).

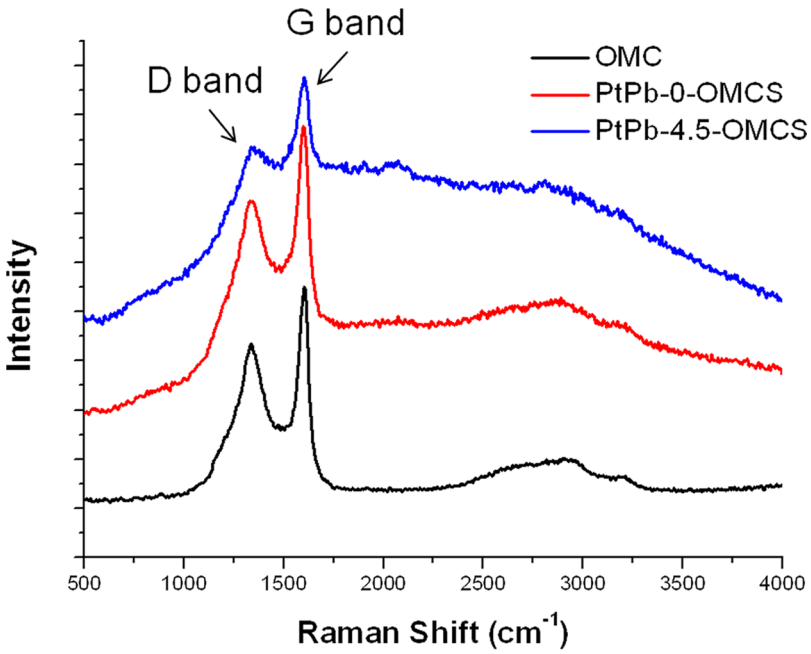

Figure 3. Raman spectroscopy of OMC, PtPb-0-OMCS, and PtPb-4.5-OMCS.

Supporting Information).[45–47] The agglomeration of nanoparticles during heat treatment at 700 °C might be minimized due to the riveted carbon originating from the PS blocks.[40]

SAXS characterization of the calcined samples clearly shows that the 2-D hexagonal, large-pore mesoporous structure is still retained after heat treatment at 700 °C (Figure 2a–c, red line). In the case of PtPb-9-OMCS, the peaks became somewhat less distinct due to the higher loading of nanoparticles within the structures, which can reflect X-rays.[48] A comparison of the SAXS patterns of calcined and as-made samples shows that peaks shifted to higher q values following calcination because of shrinkage of the framework during the removal of all volatile species and cross-linking of inorganic materials. The corresponding d_{100} values of the calcined PtPb-0-OMCS, PtPb-4.5-OMCS, and PtPb-9-OMCS are 32.3, 42.4, and 41.1 nm, respectively.

Powder XRD patterns of calcined PtPb-4.5-OMCS and PtPb-9-OMCS shown in Figure 2d reveal the formation of metal nanoparticles consisting of single phase intermetallic PtPb ($P6_3/mmc$, a = 4.24 Å, c = 5.48 Å, JCPDS-ICDD #06-0374) with Pt_xPb (JCPDS #06-0574) as a small fraction of impurities. Similar XRD patterns have been occasionally observed in previous reports in which the authors studied synthesis of intermetallic PtPb nanoparticles prepared by reducing metal–organic precursors with $NaBH_4$ or polyalcohol in the presence of oleylamine and oleic acid.[49,50] The average crystallite size of PtPb-4.5-OMCS and PtPb-9-OMCS, as calculated from the Debye–Scherrer equation,[51] was found to be 11.9 and 13.1 nm, respectively. Increasing the loading level from 4.5 to 9 wt % did not significantly increase the crystal size. Further verification of the intermetallic phase of PtPb came from high-resolution transmission electron microscope (HR-TEM) (Figure 4f) analyses. The observed lattice planes with a d-spacing of 0.219 nm were assigned to the (102) planes of intermetallic PtPb. The HR-TEM image and Fourier-transform (FT) pattern of a single PtPb nanoparticle (Figure 4g) suggest that intermetallic nanoparticles are single crystal. Inductively coupled plasma spectroscopy analysis revealed that the Pt:Pb atomic ratio was close to 1:1 (Pt: 2.18 wt %, Pb: 2.29 wt % for PtPb-4.5-OMCS and Pt: 4.42 wt %, Pb: 4.54 wt % for PtPb-9-OMCS based on carbon–silica composites, respectively). The results of scanning electron microscope (SEM) in combination with EDX (energy dispersive X-ray spectroscopy) further confirm that OMCS-supported intermetallic PtPb nanoparticles were formed successfully *via* co-reduction of metal precursors by high-temperature treatment without significant leaching of Pb and agglomeration of intermetallics (Figure S4 in the Supporting Information).

The structure of the ordered, large-pore mesoporous carbon–silica composites was also investigated by nitrogen physisorption (Figure 5). All of the PtPb-OMCS samples show typical type IV N_2 adsorption–desorption isotherms with a sharp capillary condensation at 0.95 P/P_0 and H1-type hysteresis (Figure 5a).

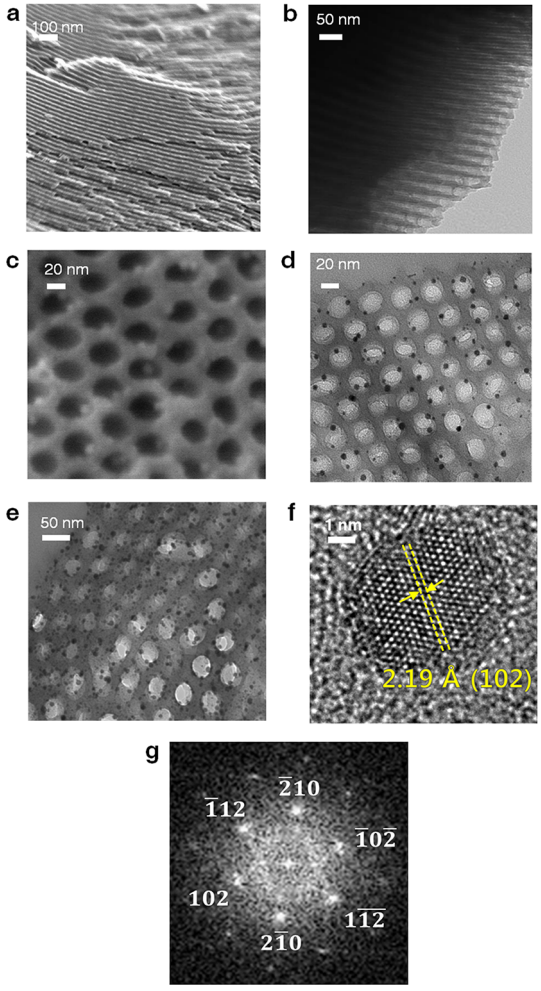

Figure 4. Characterization of materials by electron microscopy. (a, c) SEM images of (a) PtPb-0-OMCS and (c) PtPb-4.5-OMCS. (b, d, e) TEM images of (b) PtPb-0-OMCS, (d) PtPb-4.5-OMCS, and (e) PtPb-9-OMCS. (f) HR-TEM image of intermetallic PtPb nanoparticle. (g) Fourier-transform (FT) pattern of single PtPb nanoparticle along the [2 4 −1] zone axis obtained from (f).

This implies that the mesostructure of PtPb-x-OMCS exhibits cylindrical geometry, large pores, and high uniformity.[52] The pore sizes of PtPb-0-OMCS, PtPb-4.5-OMCS, and PtPb-9-OMCS estimated from the Barrett–Joyner–Halenda method[53] using the N_2 adsorption branch of the isotherm are as large as 26, 35, and 34 nm, respectively (Figure 5b). The surface areas of PtPb-0-OMCS, PtPb-4.5-OMCS, and PtPb-9-OMCS are 472, 434, and 372 m^2/g, respectively.

TEM (Figure 4b, d, e) and SEM (Figure 4a, c) images provide firm evidence of the highly ordered structure of the 2-D hexagonal PtPb-x-OMCS samples. The observed pore size of each sample was consistent with the pore size distribution analysis result of the BET measurement. PtPb nanoparticles with approximate sizes of 10 nm are located inside the ordered channels and are well-dispersed with a negligible amount of large-sized PtPb agglomerates (see also Supporting Information Figures S5 and S6). The size distribution of

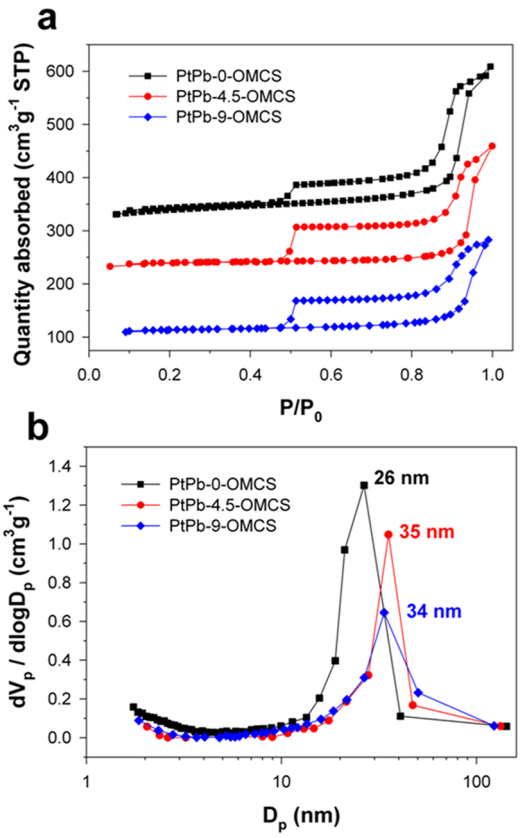

Figure 5. Characterization of materials by N_2 physisorption. (a) N_2 adsorption–desorption isotherms and (b) pore size distributions of PtPb-0-OMCS (black line), PtPb-4.5-OMCS (red line), and PtPb-9-OMCS (blue line).

nanoparticles was analyzed by counting 300 nanoparticles from the TEM images (Figure S7 in the Supporting Information). The particle sizes inferred from the TEM images are very close to those from the XRD analysis, which corroborates that most of the PtPb nanoparticles are single crystalline.[54] A slight difference between sizes of nanoparticles obtained from TEM images and those calculated from the Scherrer equation could be attributed to the presence of a small fraction of PtPb agglomerates. For comparison, in a previous report in which unsupported intermetallic PtPb nanoparticles were synthesized by a sodium borohydride reduction method at low temperature,[23] a discrepancy between the XRD and SEM/TEM analyses was found where XRD analysis indicated a crystal size of 10.6 nm, whereas the resulting particle size observed by SEM or TEM was 152 nm, due to severe aggregation of primary particles. The average size of the mesoporous composite particles was 700–800 nm (the whole distribution ranging from hundreds of nm to ~1 μm) after a light ball-mill treatment (Figure S8 in the Supporting Information). Because the metal precursors preferentially reside in the PS domains, the nanoparticles in the resulting structure should be located inside the channel-type pores. If we used the hydrophilic metal precursors, which can selectively interact with the hydrophilic PEO segments, the resulting nanoparticles would be located in the walls (Figure S9 in the Supporting Information). Even in the case of PtPb-9-OMCS, which had the highest nanoparticle loading investigated here, ordered large-pore mesostructures with well-dispersed PtPb nanoparticles were retained without structural collapse (Figure 4e).

The indispensability of laboratory-synthesized block copolymers such as PS-*b*-PEO for confining PtPb nanoparticles inside the large-pore OMCS through a simple one-pot synthesis was illustrated by comparison with a synthesis in which the commercially available block copolymer F127-$(EO)_{106}(PO)_{70}(EO)_{106}$ (hereafter referred to simply as F127) was used as the structure-directing agent. The synthesis was conducted using a similar experimental technique and under the same conditions as described in the Methods section. During the metal–copolymer assembly, hydrophobic Pt and Pb precursors were expected to be selectively incorporated into the PPO portion of the polymer, which is relatively hydrophobic. However, TEM analysis (Figure S10a in the Supporting Information) showed that most of the PtPb nanoparticles were not confined within the pores of the resulting mesoporous silica–carbon composite and the metallic particle size was larger than 30 nm. X-ray diffraction patterns (Figure S10b in the Supporting Information) of PtPb obtained by using the F127 template showed a double-phase structure consisting of PtPb (JCPDS-ICDD #06-0374) and Pt_xPb (JCPDS-ICDD #06-0574), while the crystallite size calculated from the Debye–Scherrer equation was 30.2 nm, similar to that observed by TEM. This result is consistent with the formation of bimetallic PtPb phases prepared by arc-melting under extended sintering treatment,[55] indicating that the PtPb nanoparticles are largely placed in an exposed environment due to a weak confinement effect of the PPO portion of the F127 template. Moreover, the channel size of the mesoporous carbon–silica composites formed from the F127 template is known to be smaller than 10 nm.[30] Therefore, the fact that the nanoparticles are larger than the channels of the F127-templated mesoporous carbon–silica materials can be attributed to the poor selective interaction between the PPO group and the hydrophobic metal precursors. In other words, the PPO segment of F127 was insufficiently hydrophobic to produce an efficient interaction with the hydrophobic Pt and Pb precursors. As a result, PtPb nanoparticles might be present on the outer region of the pores and agglomerate into larger crystals during heat treatment at 700 °C. These results confirm that the difference between hydrophobicity and hydrophilicity in an amphiphilic block copolymer must be sufficiently large for selective inclusion of the PtPb nanocrystals inside the pores of the OMCS, highlighting the importance of laboratory-synthesized block copolymers for

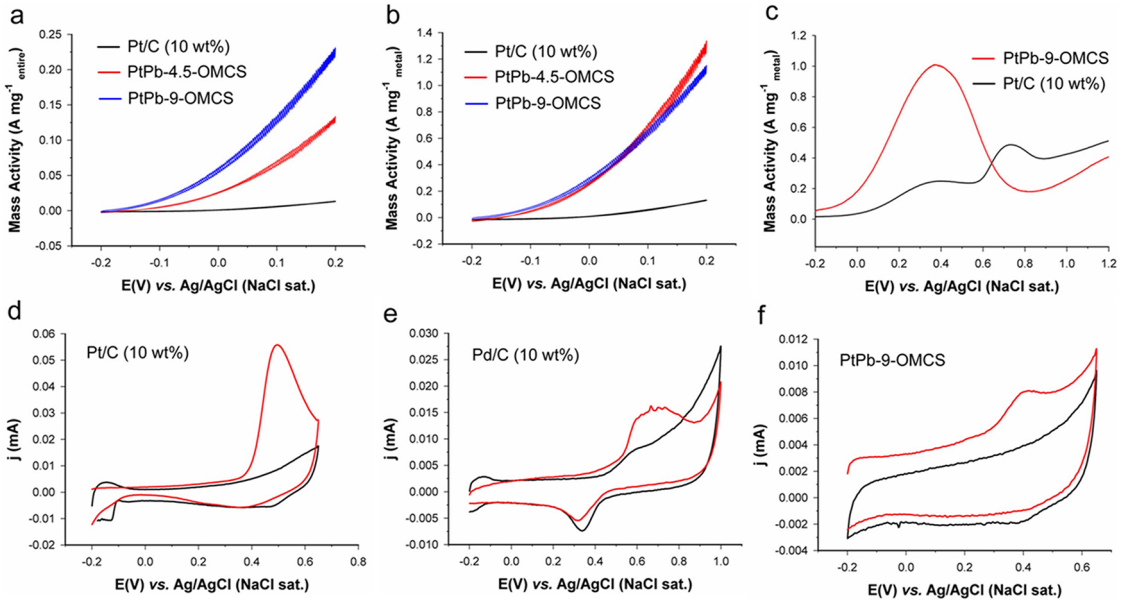

Figure 6. (a, b) Rotating-disk electrode voltammograms (10 mV s^{-1} and 2000 rpm) from Pt/C (black line), PtPb-4.5-OMCS (red line), and PtPb-9-OMCS (blue line) for formic acid oxidation measured as (a) mass activity based on loading of entire catalysts (50 μg cm^{-2}) and (b) metal nanoparticles in 0.5 M formic acid and 0.1 M H_2SO_4. (c) Steady-state cyclic voltammograms (anodic scans) of Pt/C (red line) and PtPb-9-OMCS (black line) in 0.5 M formic acid and 0.1 M H_2SO_4 at a scan rate of 10 mV s^{-1}. (d–f) CO stripping profiles obtained from (d) Pt/C, (e) Pd/C, and (f) PtPb-9-OMCS in 0.1 M H_2SO_4 aqueous solution at 10 mV s^{-1}. The black and red curves were obtained before and after CO exposure for 30 min, respectively.

facile synthesis of functional large-pore mesoporous materials.

Electrochemical Characterization. The electrocatalytic activity of the PtPb-OMCS catalysts toward formic acid oxidation was studied by cyclic voltammetry (CV). Figure 6a and b shows the rotating-disk electrode voltammograms of formic acid oxidation on PtPb-*x*-OMCS catalyst electrodes in 0.5 M formic acid and 0.1 M H_2SO_4 aqueous solution in the range −0.2 to +0.2 V (*vs* Ag/AgCl) at a potential scan rate of 10 mV s^{-1}. A commercial Pt catalyst supported on Vulcan XC-72 (10 wt %, Pt/C) was also tested under the same conditions for comparative purposes. Because the loading levels of PtPb on the OMCS are 4.5 and 9 wt %, the commercial catalyst with 10 wt % Pt/Vulcan XC-72 was chosen. The oxidation current was normalized to the entire catalyst loading (in A/mg_{entire}, Figure 6a) and metal nanoparticle loading (in A/mg_{metal}, Figure 6b), respectively. The oxidation current was doubled when the total amount of PtPb nanocatalyst increased by a factor of 2 between PtPb-4.5-OMCS and PtPb-9-OMCS. This implies that the catalytic sites in the PtPb surface region, where formic acid oxidation takes place, doubled as the total amount of catalyst doubled from 4.5% to 9%, indicating that the nanoparticles participate uniformly in the formic acid oxidation.

For high catalytic efficiency, high oxidation currents must be obtained, and therefore, the catalyst system should exhibit low overpotentials at around −0.2 V (*vs* NaCl saturated Ag/AgCl), where the onset of thermodynamic formic acid oxidation occurs.[56] The onset potential was defined as the point where the mass activity reached 0.005 A/mg.[57] PtPb-4.5-OMCS, PtPb-9-OMCS, and Pt/C exhibited onset potentials of −0.18, −0.19, and −0.03 V, respectively. The onset potentials of PtPb-4.5-OMCS and PtPb-9-OMCS were thus lower than that of Pt/C by 0.15 and 0.16 V, respectively, indicating more facile oxidation of formic acid on the intermetallic PtPb nanoparticles than on pure Pt. The mass activity values at +0.2 V for formic acid oxidation on PtPb-4.5-OMCS and PtPb-9-OMCS were 1.33 and 1.14 A/mg_{metal}, which is more than 10 times higher than that of Pt/C (0.13 A/mg_{metal}) at the same potential. In particular, PtPb-4.5-OMCS showed the highest mass activity of 1.33 A/mg_{metal} (2.66 A/mg_{pt}) at 0.2 V. Since the average size of PtPb nanoparticles is around 12 nm, the estimated oxidation current per cm^2 is 40.4 mA/cm^2, which is higher than previously reported values of bulk PtPb,[58] indicating the catalytic properties of bulk PtPb are well retained at the nanoscale. Additionally, well-dispersed (unaggregated) nanoparticles in OMCS having large 2-D hexagonal pores are beneficial for significant increases in catalytic activity for formic acid oxidation. In terms of beneficial particle size effects on electrocatalysis, 5–7 nm Pd nanoparticles are reportedly the most favorable for formic acid oxidation.[6] Considering the larger particle size of PtPb nanoparticles (10 nm) than that of commercial Pt/C (2 nm) and Pd/C (7 nm, Figure S11 in the Supporting Information), the significant increases in catalytic activity for formic acid oxidation obtained with the PtPb nanoparticles can most likely be ascribed to the high specific activity of the PtPb intermetallic phase,[22] as well as the homogeneous dispersion of

the nanoparticles inside the channel-type pore structure of the large-pore OMCS. Furthermore, the large 2-D hexagonal pores in the OMCS provide facile transport of fuels (formic acid) to the intermetallic nanocrystalline catalyst.

It is well known that the oxidation of formic acid proceeds *via* a dual-pathway mechanism[17] consisting of direct oxidation of formic acid to CO_2 at lower potential *via* dehydrogenation and the indirect pathway (or CO pathway) *via* formic acid dehydration in which CO is generated as a reaction intermediate. Because the indirect pathway requires more catalytic sites for the further oxidation of adsorbed CO at higher potential, it is generally considered an inefficient and undesirable pathway. Furthermore, CO typically poisons the Pt-based electrocatalyst.[2] Figure 6c displays the anodic oxidation profile of steady-state cyclic voltammograms of formic acid on PtPb-9-OMCS and Pt/C. For Pt/C, two distinguishable anodic peaks were observed. The second current peak at 0.73 V is much higher than the first current peak at 0.38 V, indicating that the electrochemical oxidation of formic acid on the Pt electrode occurs mainly through the undesirable dehydration pathway.[17] In other words, the Pt surface is easily blocked or poisoned by CO generated during the formic acid oxidation. For PtPb-9-OMCS, on the other hand, only one anodic peak was observed at lower potential (0.37 V), and in addition, the obtained current per unit mass of metal is 5 times higher than that of the Pt/C electrode at the same potential. This indicates that the formation of CO is almost entirely precluded on the PtPb-*x*-OMCS electrode, and formic acid oxidation proceeds mainly through the desired dehydrogenation pathway.[17]

Even though the PtPb intermetallic nanocatalyst electrochemically oxidizes formic acid mainly through the dehydrogenation pathway, it is still important to prevent CO adsorption on the PtPb intermetallic nanocatalyst since very small amounts of CO may be generated after the catalytic reaction. Figure 6d–f shows the CO stripping voltammograms of 10 wt % Pt/C, 10 wt % Pd/C, and PtPb-9-OMCS in 0.1 M H_2SO_4 solution before and after aeration with CO gas for 30 min. The black lines in all of the profiles of Figure 6d–f represent the voltammetric profile in a N_2-saturated solution of 0.1 M H_2SO_4 for the clean electrode before CO bubbling. The highest current density for CO oxidation occurs on Pt/C with a sharp peak at *ca.* +0.5 V (Figure 6d), indicating the high affinity of the Pt surfaces toward CO adsorption. On the Pd surfaces, a broad oxidation peak is observed over the potential range from +0.5 to +0.9 V (Figure 6e), and the onset potential of CO oxidation was 0.17 V higher than that of Pt/C. The broader CO oxidation peak at higher potential on Pd/C is due to the oxidation of strongly absorbed CO to CO_2. In the case of PtPb-9-OMCS (Figure 6f), the current density of CO stripping is much weaker than that of pure Pt/C and Pd/C, suggesting that PtPb-9-OMCS exhibits a much higher resistance toward CO adsorption than both Pt/C and Pd/C. The lower onset potential compared with Pt/C and Pd/C indicates that even if there is a negligible amount of absorbed CO, it can be easily and rapidly oxidized to CO_2. The dramatic enhancement of CO tolerance on the PtPb-9-OMCS electrode could be ascribed to the expanded Pt–Pt distance of Pt ions on the intermetallic PtPb surfaces relative to pure Pt, which results in inhibition of CO adsorption at bridges and 3-fold hollow sites.[57] In the PtPb-*x*-OMCS electrode, a very small amount of CO will be generated during fuel cell operation because the PtPb intermetallic phase catalyzes the oxidation of formic acid to CO_2 by the direct pathway. This small amount of CO will not be adsorbed onto the PtPb intermetallic nanocrystals and, thus, should not affect the electrode performance of PtPb-*x*-OMCS. The minimized formation of CO by the dehydration pathway and negligible CO poisoning on PtPb-*x*-OMCS should lead to enhanced catalytic performance when it is used as a real fuel cell catalyst in single-cell systems. Using the CO stripping method, the electrochemical active surface area (EASA) can be measured in the case of Pt nanocatalysts. However, intermetallic PtPb catalysts show very poor affinity, as shown in Figure 6f. Therefore, EASA cannot be calculated from the peak charge of CO in the present case.[58]

The stability of the catalysts was examined by chronoamperometry in formic acid oxidation at 0.3 V *vs* Ag/AgCl. As shown in Figure S12, the current for formic acid oxidation of PtPb-9-OMCS slowly decreases to preserve about 50% of its initial activity. In contrast, the Pd/C and Pt/C catalysts lost more than 50% of their initial activity within five minutes. Moreover, PtPb-9-OMCS shows a higher initial activity (1.56 A/mg_{metal}) and a lower deactivation rate of 4.4%/100 s after 1000 s than Pt/C and Pd/C, for which the initial activities were 0.16 and 0.31 A/mg_{metal} and the deactivation rates were 5.1 and 9.2%/100 s after 1000 s, respectively. The deactivation rate of PtPb-9-OMCS is comparable to that of previously reported PtBi/OMC over the same period.[28] The rapid degradation rate of the oxidation current on Pt/C and Pd/C seems to be due to CO poisoning, whereas the slower deactivation rate of PtPb-9-OMCS indicates the better resistivity toward CO poisoning. After 1 h, the mass activity of PtPb-9-OMCS (based on metal) for formic oxidation was 7 and 30 times higher than those of Pt/C and Pd/C, respectively. This confirms that the simple one-pot method for synthesis of intermetallics on large-pore OMCSs presented herein could be an effective route to achieving both high catalytic activity and stability.

Incorporation of Pt-based catalysts into the small pores of CMK-3 carbon (pore size <5 nm) would inhibit the formation of the TPB phase because the micelle structure formed from ionic clusters present in the

Nafion membrane is known to be larger than 4 nm.[59] In contrast, the pore size of PtPb-*x*-OMCS is larger than 30 nm even after catalyst loading, which is favorable for the formation of TPB sites. Although it is very difficult to confirm that Nafion is fully penetrating into the pores, electron energy loss spectroscopy (EELS) maps of sulfur on Nafion/PtPb-9-OMCS showed sulfur is distributed within the channels of PtPb-9-OMCS (Figure S13 in the Supporting Information). This observation suggests that Nafion ionomers containing sulfonic acid groups were successfully infiltrated into the pores of PtPb-9-OMCS. The nanocrystalline PtBi-incorporated CMK-3 support with small pore size was not tested as an anode catalyst in a real fuel cell.[24]

In the present study, PtPb-9-OMCS, commercially available Pt/C, and Pd/C were tested as electrocatalysts in the anode of the DFAFC by using 5 M formic acid. The DFAFC test was performed using two MEAs of each sample to check the reliability and the reproducibility (Figure S14 in the Supporting Information). Figure 7 shows the *I*−*V* curves of PtPb-9-OMCS, Pt/C, and Pd/C catalyst with power density performance at temperatures of 30, 40, and 50 °C. An open circuit voltage of *ca.* 0.9 V was observed for all three samples. The maximum power density of PtPb-9-OMCS at 50 °C was 239.8 mW/mg_{PtPb}, which is 53% higher than that of the commercial Pt/C (156.63 mW/mg_{Pt}). Pd/C (256.24 mW/mg_{Pd}) showed a slightly higher power density than PtPb-9-OMCS (Figure 7c). However, Pd/C exhibited rapid degradation above 550 mA/mg_{Pd}. In other words, Pd/C catalyst is unstable in the high current density region, which is related to poisoning of Pd catalyst in formic acid fuel. In general, catalyst support materials are important for the performance of fuel cells because they provide mass transport of fuels and reactants, electrochemical active area, *etc.*[60,61] The large-pore OMCS offers effective mass transport and high rate of formic acid oxidation due to the ordered large-pore channel structure with large surface area. As a result, the maximum current density of PtPb-9-OMCS measured at 0.25 V was 941.11 mA/mg_{PtPb}, which is much higher than those of Pd/C (715.43 mA/mg_{Pd}) and Pt/C catalysts (491.31 mA/mg_{Pt}). These results indicate that the ordered large-pore mesoporous carbon−silica structure and intermetallic PtPb catalyst particles of PtPb-9-OMCS contribute to the enhanced formic acid fuel cell performance.

It is practically important to compare the power density at 0.4 V, which is a typical voltage of DFAFC operating conditions.[62,63] Thus, we compared the power density of each MEA at 0.4 V. Power densities were 210 mW/mg_{PtPb} for PtPb-9-OMCs, 83 mW/mg_{Pt} for Pt/C, and 241 mW/mg_{Pd} for Pd/C, respectively. Pd/C showed somewhat higher power density than PtPb-9-OMCS catalyst at 0.4 V and 50 °C. However, the stability performance of catalysts is important and should be considered in practical applications of DFAFC.

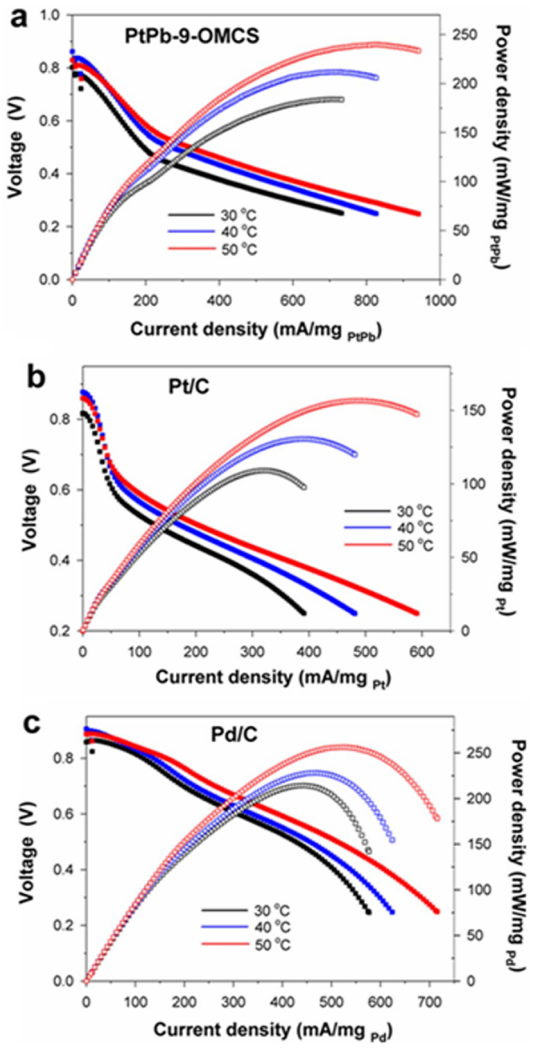

Figure 7. *I*−*V* curves with power density plots at 30, 40, and 50 °C of (a) PtPb-9-OMCS, (b) Pt/C (10 wt %), and (c) Pd/C (10 wt %).

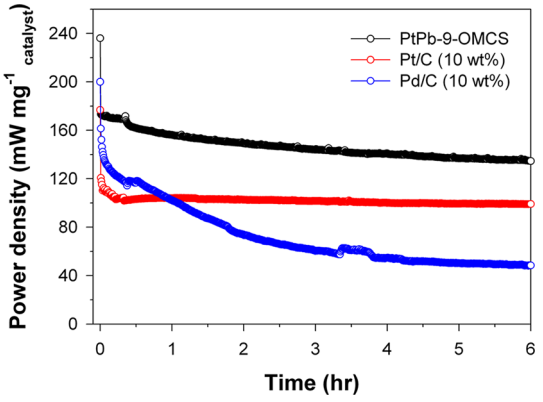

Figure 8. Time dependence of power density at a fuel cell voltage of 0.4 V.

To confirm the stability performance of three catalysts, MEA stability tests were performed by applying constant voltage (0.4 V) to cells for 6 h at 50 °C (Figure 8). Pd/C has the highest performance among the catalysts at the onset point, but the degradation

rate of the power density is the highest, decaying from 245.01 to 48.38 mW/mg$_{Pd}$ during 6 h. Thus the activity of Pd/C is good at very short times, but this catalyst has poor stability in formic acid fuel cells over long times, since Pd is easily poisoned by unknown organic species.[13] In contrast, the PtPb-9-OMCS catalyst, having enhanced tolerance for CO poisoning, shows more stable performance compared with Pd/C (PtPb-9-OMCS stability performance: 236.08 (initial) to 134.51 mW/mg$_{PtPb}$ after 6 h). Although Pt/C shows the most stable performance, the initial power density is lowest (120.65 mW/mg$_{Pt}$) and the power density after 6 h is also lower than that of PtPb-9-OMCS.

When we further increase the single-cell operation temperature to 60 °C, the power density of the PtPb-9-OMCS catalyst measured at 0.4 V was 273 mW/mg$_{PtPb}$, higher than those of Pt/C (148 mW/mg$_{Pt}$) and Pd/C (233 mW/mg$_{Pd}$) (see Figure S15 in the Supporting Information).

The single-cell performance results suggest that the presented PtPb-*x*-OMCS catalysts may be practically applied as real fuel cell catalysts for DFAFC.

CONCLUSIONS

In conclusion, a one-pot process rather than tedious multistep procedures was employed to successfully prepare ordered (2D hexagonal) large-pore (>30 nm) mesoporous carbon/silica composites with highly dispersed intermetallic PtPb nanocatalysts for use as anode catalysts in DFAFCs. The block copolymer PS-*b*-PEO used in this work was synthesized by atom transfer radical polymerization (ATRP), a polymerization technique that makes block copolymer synthesis, and preparation of large-pore mesoporous materials from it, widely accessible, *i.e.*, also to nonexperts. Having sufficient contrast between the hydrophobic (PS) and hydrophilic (PEO) blocks, amphiphilic PS-*b*-PEO is key to the successful confinement of intermetallic nanoparticle formation within the OMCS pores (or channels) without agglomeration or incorporation in the support walls. The resulting PtPb-*x*-OMCS materials showed both superior mass activity and higher stability for formic acid oxidation than commercial Pt/C and Pd/C catalysts. The quality of the resulting anode catalysts was further tested under realistic DFAFC (single-cell) conditions rather than merely by half-cell electrochemical characterization. Despite larger nanoparticle size, the resulting anode catalysts outperformed commercial Pt/C and Pd/C catalysts. This result was attributed to the combination of both the intermetallic PtPb nanoparticle phase as well as their significantly smaller size compared to the pore diameters of the support, allowing formation of the desired triple phase boundary through efficient mass transport of ionomer (Nafion) and fuel through the pores. It is expected that this simple methodology can be extended to the preparation of other intermetallic nanoparticles inside large-pore mesoporous materials. The composites prepared by this method may find use in a wide range of applications including solar cells, biofuel cells, and batteries.

METHODS

Synthesis of PtPb-OMCSs. The copolymer PS-*b*-PEO (PDI: 1.09) with M_n = 43 000 g mol^{-1} and 10 wt % PEO was synthesized by ATRP. A typical procedure for the synthesis of PtPb-4.5-OMCS was as follows: 0.15 g of PS-*b*-PEO was dissolved in a mixture of THF (3.75 g) and $CHCl_3$ (3.75 g). Equimolar amounts of dimethyl-(1,5-cyclooctadiene)platinum(II) (15 mg, Strem Chemicals) and triphenyl(phenylethynyl)lead (97%) (24 mg, Sigma-Aldrich) were added to the polymer solution. TEOS (0.292 g, Sigma-Aldrich), 0.1 M HCl solution (0.07 mL), and resol solution (1.65 g, 10 w/v in THF) were added to the polymer−metal precursor solution. After stirring for 1 h at room temperature, the solution was poured into a Petri dish. The as-made film was collected by evaporation of solvents on a hot plate at 50 °C and further annealed at 100 °C. Subsequent heat treatment was carried out in a furnace at 450 °C for 3 h and subsequently at 700 °C for 2 h under 4% H_2/Ar. The heating rate was 1 °C/min. For the synthesis of PtPb-9-OMCS, 34.5 mg of Pt precursor and 53.2 mg of Pb precursor were added to the polymer solution. PtPb-0-OMCS was prepared without metal precursors using the same procedure.

Characterization. Small-angle X-ray scattering experiments were carried out on the 4C1 SAXS station at the Pohang Accelerator Laboratory (PAL, Korea). Powder X-ray diffraction (XRD) patterns were obtained with a Rigaku D/Max-2500 diffractometer using Cu Kα radiation (λ = 1.5418 Å) at a scanning rate of 4.0 deg min^{-1}. Morphological investigations were carried out using a transmission electron microscope (Hitachi H-7600) operated at 100 kV and a scanning electron microscope (Hitachi S-4800). HR-TEM images were obtained with a JEOL JEM-2200FS instrument operated at 200 kV. The surface areas of the prepared samples were calculated from the 77 K N_2 adsorption−desorption isotherms using a Tristar II 3020 system (Micromeritics Inc.). Inductively coupled plasma spectroscopy was used to measure the actual loading amount of Pt and Pb nanoparticles in the OMCSs.

Electrochemical Measurements. The catalytic ink for preparation of working electrodes consisted of 8 mg of PtPb-OMCS catalyst dispersed in a mixture of 3.18 mL of ultrapure water, 0.8 mL of 2-propanol, and 20 μL of a 5% w/w alcoholic solution of Nafion (Aldrich). A 25 μL amount of ink was dropped onto the surface of a glassy carbon electrode (GCE) with 6 mm diameter and then dried under ambient atmosphere. The surface of the GCE contained 50 μg of the catalyst. A commercial Pt/C (10% Pt on Vulcan-XC, Premetek Co.) and Pd/C (10% Pd on activated carbon, Aldrich) electrodes were prepared by the same method. The catalyst-coated GCEs were rotated at 2000 rpm to minimize the possible blockage of catalytic active sites on the surface by bubbles formed during FA oxidation. CV measurements were performed for formic acid oxidation at a scan rate of 10 mV s^{-1} in an aqueous solution of 0.1 M H_2SO_4 containing 0.5 M formic acid in the range −0.2 to +0.2 V (*vs* Ag/AgCl).

CO stripping measurements were carried out in 0.1 M H_2SO_4 aqueous solution. Prior to CO exposure, the H_2SO_4 solution was purged with nitrogen gas for 30 min to freshen the catalyst-coated GCE. The solution was then ventilated with high-purity CO gas (99.9%) for 30 min while keeping the electrode potential at −0.12 V. After bubbling with nitrogen gas for 30 min to remove the dissolved CO, the electrode potential was still maintained at −0.12 V. Finally, CO stripping voltammograms were obtained at a scan rate of 10 mV s^{-1} in the potential range between −0.2 and +0.65 V in a N_2-saturated 0.1 M H_2SO_4 solution.[57] The electrode potentials for all electrochemical

measurements were referenced to a NaCl-saturated Ag/AgCl electrode.

Catalyst slurries were prepared for single-cell tests by dispersing the three catalysts (PtPb-9-OMCS, Pd/C, and Pt/C) into appropriate amounts of ultrapure water, 10% Nafion water base solution, 1-propanol, and 2-propanol. The MEAs with an active area of 3 cm^2 were fabricated by using a brushing method to apply the catalyst layer on the carbon paper as electrodes and hot-pressing a 115 Nafion membrane sandwiched by the anode and cathode layer. The cathode consisted of commercial 40 wt % platinum carbon (HISPEC 4000, Johnson Matthey Co.) with loading amounts of 4 mg/cm^2. The anode consisted of catalyst particles at the following loadings: 1.2 mg cm^{-2} for PtPb-OMCS and Pd/C; 1.67 mg cm^{-2} for Pt/C. The MEA performance was evaluated for each of the different anode catalysts with 5 M formic acid at a flow rate of 3.5 mL/min. Air was supplied to the cathode at a flow rate of 200 cm^3/min.

Conflict of Interest: The authors declare no competing financial interest.

Acknowledgment. This work was supported by a National Research Foundation of Korea Grant funded by the Korean Government (2010-0015244 and 2010-0027729). This work was also financially supported by the Korean Ministry of Knowledge Economy through the New and Renewable Energy Center under Contract Number 2008-N-FC08-P-01 and by the second stage of the BK 21 program of Korea. This work was further supported by the Global Frontier R&D Program on Center for Multiscale Energy System, which was funded by the National Research Foundation under the Ministry of Education, Science and Technology, Korea. U.W. gratefully acknowledges financial support of the Energy Materials Center at Cornell (EMC2), an Energy Frontier Research Center funded by the U.S. Department of Energy, Office of Science, Office of Basic Energy Sciences, under Award No. DE-SC0001086.

Supporting Information Available: Powder XRD patterns of PtPb-9-OMCS heat-treated at 450 °C in H_2/N_2 atmosphere. Conductivity measurement of PtPb-4.5-OMCS. SEM/EDX of PtPb-4.5-OMCS. Size distribution of PtPb nanoparticles. TEM image and powder XRD pattern of PtPb−carbon−silica composite after heat treatment at 700 °C using commercially available block copolymer (F127). Chronoamperometry curves of PtPb-9-OMCS, Pd/C, and Pt/C. TEM images and powder XRD patterns of commercial Pt/C and Pd/C. HR-TEM images of original and EELS sulfur mapping of PtPb-9-OMCS with Nafion ionomer. This material is available free of charge *via* the Internet at http://pubs.acs.org.

REFERENCES AND NOTES

1. Kang, S.; Lee, J.; Lee, J. K.; Chung, S.-Y.; Tak, Y. Influence of Bi Modification of Pt Anode Catalyst in Direct Formic Acid Fuel Cells. *J. Phys. Chem. B* **2006**, *110*, 7270–7274.
2. Rice, C.; Ha, S.; Masel, R. I.; Waszczuk, P.; Wieckowski, A.; Barnard, T. Direct Formic Acid Fuel Cells. *J. Power Sources* **2002**, *111*, 83–89.
3. Uhm, S.; Lee, H. J.; Kwon, Y.; Lee, J. A Stable and Cost Effective Anode Catalyst Structure for Formic Acid Fuel Cells. *Angew. Chem., Int. Ed.* **2008**, *120*, 10317–10320.
4. Qian, W.; Wilkinson, D. P.; Shen, J.; Wang, H.; Zhang, J. Architecture for Portable Direct Liquid Fuel Cells. *J. Power Sources* **2006**, *154*, 202–213.
5. Zhou, W.; Lee, J. Y. Highly Active Core-Shell Au@Pd Catalyst for Formic Acid Electrooxidation. *Electrochem. Commun.* **2007**, *9*, 1725–1729.
6. Zhou, W.; Lee, J. Y. Particle Size Effects in Pd-Catalyzed Electrooxidation of Formic Acid. *J. Phys. Chem. C* **2008**, *112*, 3789–3793.
7. Baldauf, M.; Kolb, D. M. Formic Acid Oxidation on Ultrathin Pd Films on Au (hkl) and Pt (hkl) Electrodes. *J. Phys. Chem.* **1996**, *100*, 11375–11381.
8. Jiang, J.; Kucernak, A. Nanostructured Platinum as an Electrocatalyst for the Electrooxidation of Formic Acid. *J. Electroanal. Chem.* **2002**, *520*, 64–70.
9. Waszczuk, P.; Barnard, T. M.; Rice, C.; Masel, R. I.; Wieckowski, A. A Nanoparticle Catalyst with Superior Activity for Electrooxidation of Formic Acid. *Electrochem. Commun.* **2002**, *4*, 599–603.
10. Arenz, M.; Stamenkovic, V.; Schmidt, T. J.; Wandelt, K.; Ross, P. N.; Markovic, N. M. The Electro-Oxidation of Formic Acid on Pt-Pd Single Crystal Bimetallic Surfaces. *Phys. Chem. Chem. Phys.* **2003**, *5*, 4242–4251.
11. Miyake, H.; Okada, T.; Samjeské, G.; Osawa, M. Formic Acid Electrooxidation on Pd in Acidic Solutions Studied by Surface-Enhanced Infrared Absorption Spectroscopy. *Phys. Chem. Chem. Phys.* **2008**, *10*, 3662–3669.
12. Wang, J.-Y.; Kang, Y.-Y.; Yang, H.; Cai, W.-B. Boron-Doped Palladium Nanoparticles on Carbon Black As a Superior Catalyst for Formic Acid Electro-Oxidation. *J. Phys. Chem. C* **2009**, *113*, 8366–8372.
13. Yu, X.; Pickup, P. G. Recent Advances in Direct Formic Acid Fuel Cells (DFAFC). *J. Power Sources* **2008**, *182*, 124–132.
14. Chen, Y. X.; Heinen, M.; Jusys, Z.; Behm, R. J. Kinetics and Mechanism of the Electrooxidation of Formic Acid—Spectroelectrochemical Studies in a Flow Cell. *Angew. Chem., Int. Ed.* **2006**, *45*, 981–985.
15. Lović, J. D.; Tripković, A. V.; Gojković, S. Lj.; Popović, K. Dj.; Tripković, D. V.; Olszewski, P.; Kowal, A. Kinetic Study of Formic Acid Oxidation on Carbon-Supported Platinum Electrocatalyst. *J. Electroanal. Chem.* **2005**, *581*, 294–302.
16. Haan, J. L.; Masel, R. I. The Influence of Solution pH on Rates of an Electrocatalytic Reaction: Formic Acid Electrooxidation on Platinum and Palladium. *Electrochim. Acta* **2009**, *54*, 4073–4078.
17. Parsons, R.; VanderNoot, T. The Oxidation of Small Organic Molecules: A Survey of Recent Fuel Cell Related Research. *J. Electroanal. Chem.* **1988**, *257*, 9–45.
18. Uhm, S.; Chung, S.; Lee, J. Activity of Pt Anode Catalyst Modified by Underpotential Deposited Pb in a Direct Formic Acid Fuel Cell. *Electrochem. Commun.* **2007**, *9*, 2027–2031.
19. Yang, Y.-Y.; Sun, S.-G. Effects of Sb Adatoms on Kinetics of Electrocatalytic Oxidation of HCOOH at Sb-Modified Pt (100), Pt (111), Pt (110), Pt (320), and Pt (331) Surfaces−An Energetic Modeling and Quantitative Analysis. *J. Phys. Chem. B* **2002**, *106*, 12499–12507.
20. Yu, X.; Pickup, P. G. Novel Pd−Pb/C Bimetallic Catalysts for Direct Formic Acid Fuel Cells. *J. Power Sources* **2009**, *192*, 279–284.
21. Chen, D.-J.; Zhou, Z.-Y.; Wang, Q.; Xiang, D.-M.; Tian, N.; Sun, S.-G. A Non-Intermetallic PtPb/C Catalyst of Hollow Structure with High Activity and Stability for Electrooxidation of Formic Acid. *Chem. Commun.* **2010**, *46*, 4252–4254.
22. Casado-Rivera, E.; Volpe, D. J.; Alden, L.; Lind, C.; Downie, C.; Vazquez-Alvarez, T.; Angelo, A. C. D.; DiSalvo, F. J.; Abruna, H. D. Electrocatalytic Activity of Ordered Intermetallic Phases for Fuel Cell Applications. *J. Am. Chem. Soc.* **2004**, *126*, 4043–4049.
23. Roychowdhury, C.; Matsumoto, F.; Zeldovich, V. B.; Warren, S. C.; Mutolo, P. F.; Ballesteros, M. J.; Wiesner, U.; Abruna, H. D.; DiSalvo, F. J. Synthesis, Characterization, and Electrocatalytic Activity of PtBi and PtPb Nanoparticles Prepared by Borohydride Reduction in Methanol. *Chem. Mater.* **2006**, *18*, 3365–3372.
24. Ji, X.; Lee, K. T.; Holden, R.; Zhang, L.; Zhang, J.; Botton, G. A.; Couillard, M.; Nazar, L. F. Nanocrystalline Intermetallics on Mesoporous Carbon for Direct Formic Acid Fuel Cell Anodes. *Nat. Chem.* **2010**, *2*, 286–293.
25. Radmilovic, V.; Gasteiger, H. A.; Ross, P. N. Structure and Chemical Composition of a Supported Pt-Ru Electrocatalyst for Methanol Oxidation. *J. Catal.* **1995**, *154*, 98–106.
26. Lee, J.; Kim, J.; Hyeon, T. Recent Progress in the Synthesis of Porous Carbon Materials. *Adv. Mater.* **2006**, *18*, 2073–2094.
27. Lee, J.; Orilall, M. C.; Warren, S. C.; Kamperman, M.; DiSalvo, F. J.; Wiesner, U. Direct Access to Thermally Stable and Highly Crystalline Mesoporous Transition-Metal Oxides with Uniform Pores. *Nat. Mater.* **2008**, *7*, 222–228.
28. Orilall, M. C.; Matsumoto, F.; Zhou, Q.; Sai, H.; Abruna, H. D.; DiSalvo, F. J.; Wiesner, U. One-Pot Synthesis of

Platinum-Based Nanoparticles Incorporated into Mesoporous Niobium Oxide-Carbon Composites for Fuel Cell Electrodes. *J. Am. Chem. Soc.* **2009**, *131*, 9389–9395.
29. Kang, E.; Jung, H.; Park, J.-G.; Kwon, S.; Shim, J.; Sai, H.; Wiesner, U.; Kim, J. K.; Lee, J. Block Copolymer Directed One-Pot Simple Synthesis of L_{10}-Phase FePt Nanoparticles inside Ordered Mesoporous Aluminosilicate/Carbon Composites. *ACS Nano* **2011**, *5*, 1018–1025.
30. Liu, R.; Shi, Y.; Wan, Y.; Meng, Y.; Zhang, F.; Gu, D.; Chen, Z.; Tu, B.; Zhao, D. Triconstituent Co-Assembly to Ordered Mesostructured Polymer-Silica and Carbon-Silica Nanocomposites and Large-Pore Mesoporous Carbons with High Surface Areas. *J. Am. Chem. Soc.* **2006**, *128*, 11652–11662.
31. Tang, H.; Jiang, S. P. Self-Assembled Pt/Mesoporous Silica-Carbon Electrocatalysts for Elevated-Temperature Polymer Electrolyte Membrane Fuel Cells. *J. Phys. Chem. C* **2008**, *112*, 19748–19755.
32. Zeng, J.; Zhou, Y.; Li, L. Phosphotungstic Acid Functionalized Silica Nanocomposites with Tunable Bicontinuous Mesoporous Structure and Superior Proton Conductivity and Stability for Fuel Cells. *Phys. Chem. Chem. Phys.* **2011**, *13*, 10249–10257.
33. Meng, Y.; Gu, D.; Zhang, F.; Shi, Y.; Yang, H.; Li, Z.; Yu, C.; Tu, B.; Zhao, D. Ordered Mesoporous Polymers and Homologous Carbon Frameworks: Amphiphilic Surfactant Templating and Direct Transformation. *Angew. Chem., Int. Ed.* **2005**, *117*, 7215–7221.
34. Templin, M.; Franck, A.; Chesne, D. A.; Leist, H.; Zhang, Y.; Ulrich, R.; Schadler, V.; Wiesner, U. Organically Modified Aluminosilicate Mesostructures from Block Copolymer Phases. *Science* **1997**, *278*, 1795–1798.
35. Brinker, C. J.; Lu, Y.; Sellinger, A.; Fan, H. Evaporation-Induced Self-Assembly: Nanostructures Made Easy. *Adv. Mater.* **1999**, *11*, 579–585.
36. Wang, J. S.; Matyjaszewski, K. Controlled/"Living" Radical Polymerization. Atom Transfer Radical Polymerization in the Presence of Transition-Metal Complexes. *J. Am. Chem. Soc.* **1995**, *117*, 5614–5615.
37. Deng, Y.; Liu, J.; Liu, C.; Gu, D.; Sun, Z.; Wei, J.; Zhang, J.; Zhang, L.; Tu, B.; Zhao, D. Ultra-Large-Pore Mesoporous Carbons Templated from Poly(ethylene oxide)-*b*-polystyrene Diblock Copolymer by Adding Polystyrene Homopolymer as a Pore Expander. *Chem. Mater.* **2008**, *20*, 7281–7286.
38. Deng, Y.; Yu, T.; Wan, Y.; Shi, Y.; Meng, Y.; Gu, D.; Zhang, L.; Huang, Y.; Liu, C.; Wu, X.; *et al*. Ordered Mesoporous Silicas and Carbons with Large Accessible Pores Templated from Amphiphilic Diblock Copolymer Poly(ethylene oxide)-*b*-polystyrene. *J. Am. Chem. Soc.* **2007**, *129*, 1690–1697.
39. Hwang, J.; Kim, J.; Ramasamy, E.; Choi, W.; Lee, J. Easy Access to Highly Crystalline Mesoporous Transition-Metal Oxides with Controllable Uniform Large Pores by Using Block Copolymers Synthesized *via* Atom transfer Radical Polymerization. *Microporous Mesoporous Mater.* **2011**, *143*, 149–156.
40. Jiang, Z.-Z.; Wang, Z.-B.; Gu, D.-M.; Smotkin, E. S. Carbon Riveted Pt/C Catalyst with High Stability Prepared by *in Situ* Carbonized Glucose. *Chem. Commun.* **2010**, *46*, 6998–7000.
41. Schwan, J.; Ulrich, S.; Batori, V.; Ehrhardt, H.; Silva, S. R. P. Raman Spectroscopy on Amorphous Caron Films. *J. Appl. Phys.* **1996**, *80*, 440–447.
42. Filik, J. Raman Spectroscopy: A Simple, Non-Destructive Way to Characterise Diamond and Diamond-Like Materials. *Spectrosc. Eur.* **2005**, *17*, 10–17.
43. Min, M.; Cho, J.; Cho, K.; Kim, H. Particle Size and Alloying Effects of Pt-Based Alloy Catalysts for Fuel Cell Applications. *Electrochim. Acta* **2000**, *45*, 4211–4217.
44. Kamiuchi, N.; Matsui, T.; Kikuchi, R.; Eguchi, K. Nanoscopic Observation of Strong Chemical Interaction between Pt and Tin Oxide. *J. Phys. Chem. C* **2007**, *111*, 16470–16476.
45. Ozaki, J.; Mitsui, M.; Nishiyama, Y.; Cashion, J. D.; Brown, L. J. Effects of Ferrocene on Production of High Performance Carbon Electrodes from Poly(furfuryl alcohol). *Chem. Mater.* **1998**, *10*, 3386–3392.
46. Yoon, S.; Lee, J.; Hyeon, T.; Oh, S. M. Electric Double-Layer Capacitor Performance of a New Mesoporous Carbon. *J. Electrochem. Soc.* **2000**, *147*, 2507–2512.
47. Kang, E.; An, S.; Yoon, S.; Kim, J. K.; Lee, J. Ordered mesoporous WO_{3-X} Possessing Electronically Conductive Framework Comparable to Carbon Framework toward Long-Term Stable Cathode Supports for Fuel Cells. *J. Mater. Chem.* **2010**, *20*, 7416–7421.
48. Warren, B. E. *X-ray Diffraction*; Dover Pubns: New York, 1990.
49. Alden, L. R.; Han, D. K.; Matsumoto, F.; Abruna, H. D.; DiSalvo, F. J. Intermetallic PtPb Nanoparticles Prepared by Sodium Naphthalide Reduction of Metal-Organic Precursors: Electrocatalytic Oxidation of Formic Acid. *Chem. Mater.* **2006**, *18*, 5591–5596.
50. Liu, Z.; Guo, B.; Tay, S. W.; Hong, L.; Zhang, X. Physical and Electrochemical Characterizations of PtPb/C Catalyst Prepared by Pyrolysis of Platinum(II) and Lead(II) Acetylacetonate. *J. Power Sources* **2008**, *184*, 16–22.
51. Krawitz, A. D. *Introduction to Diffraction in Materials Science and Engineering*; Wiley: New York, 2001; p 168.
52. Kruk, M.; Jaroniec, M. Gas Adsorption Characterization of Ordered Organic-Inorganic Nanocomposite Materials. *Chem. Mater.* **2001**, *13*, 3169–3183.
53. Barrett, E. P.; Joyner, L. G.; Halenda, P. P. The Determination of Pore Volume and Area Distributions in Porous Substances. I. Computations from Nitrogen Isotherms. *J. Am. Chem. Soc.* **1951**, *73*, 373–380.
54. Park, J.; Lee, E.; Hwang, N.-M.; Kang, M.; Kim, S. C.; Hwang, Y.; Park, J.-G.; Noh, H.-J.; Kim, J.-Y.; Park, J.-H.; *et al*. One Nanometer Scale Size Controlled Synthesis of Monodisperse Magnetic Iron Oxide Nanoparticles. *Angew. Chem., Int. Ed.* **2005**, *117*, 2932–2937.
55. Zhang, L. J.; Wang, Z. Y.; Xia, D. G. Bimetallic PtPb for Formic Acid Electro-Oxidation. *J. Alloys Compd.* **2006**, *426*, 268–271.
56. Alden, L. R.; Roychowdhury, C.; Matsumoto, F.; Han, D. K.; Zeldovich, V. B.; Abruna, H. D.; DiSalvo, F. J. Synthesis, Characterization, and Electrocatalytic Activity of PtPb Nanoparticles Prepared by Two Synthetic Approaches. *Langmuir* **2006**, *22*, 10465–10471.
57. Matsumoto, F.; Roychowdhury, C.; DiSalvo, F. J.; Abruna, H. D. Electrocatalytic Activity of Ordered Intermetallic PtPb Nanoparticles Prepared by Borohydride Reduction toward Formic Acid Oxidation. *J. Electrochem. Soc.* **2008**, *155*, B148–B154.
58. Volpe, D.; Casado-Rivera, E.; Alden, L.; Lind, C.; Hagerdon, K.; Downie, C.; Korzeniewski, C.; DiSalvo, F. J.; Abruna, H. D. Surface Treatment Effects on the Electrocatalytic Activity and Characterization of Intermetallic Phases. *J. Electrochem. Soc.* **2004**, *151*, A971–A977.
59. An, S.; Park, J.-H.; Shin, C.-H.; Joo, J.; Ramasamy, E.; Hwang, J.; Lee, J. Well-Dispersed Pd_3Pt_1 Alloy Nanoparticles in Large Pore Sized Mesocellular Carbon Foam for Improved Methanol-Tolerant Oxygen Reduction Reaction. *Carbon* **2010**, *49*, 1108–1117.
60. Liu, H.; Song, C.; Zhang, L.; Zhang, J.; Wang, H.; Wilkinson, D. P. A Review of Anode Catalysis in the Direct Methanol Fuel Cell. *J. Power Sources* **2006**, *155*, 95–110.
61. Li, W.; Liang, C.; Zhou, W.; Qiu, J.; Zhou, Z.; Sun, G.; Xin, Q. Preparation and Characterization of Multiwalled Carbon Nanotube-Supported Platinum for Cathode Catalysts of Direct Methanol Fuel Cells. *J. Phys. Chem. B* **2003**, *107*, 6292–6299.
62. Park, Y.-C.; Peck, D.-H.; Kim, S.-K.; Lim, S.; Jung, D.-H.; Jang, J.-H.; Lee, D.-Y. Dynamic Response and Long-Term Stability of a Small Direct Methanol Fuel Cell Stack. *J. Power Sources* **2010**, *195*, 4080–4089.
63. Kang, S.; Lim, S.; Peck, D.-H.; Kim, S.-K.; Jung, D.-H.; Hong, S.-H.; Jung, H.-G.; Shul, Y. Stability and Durability of PtRu Catalysts Supported on Carbon Nanofibers for Direct Methanol Fuel Cells. *Int. J. Hydrogen Energy* **2012**, *37*, 4685–4693.